

1    **Stress Induced Structural Transformations in Au Nanocrystals**

2    *Abhinav Parakh<sup>1</sup>, Sangryun Lee<sup>2</sup>, Mehrdad T. Kiani<sup>1</sup>, David Doan<sup>3</sup>, Martin Kunz<sup>4</sup>, Andrew*  
3    *Doran<sup>4</sup>, Seunghwa Ryu<sup>2</sup> and X. Wendy Gu<sup>3\*</sup>*

4    <sup>1</sup>Materials Science and Engineering, Stanford University, Stanford, CA 94305, USA.

5    <sup>2</sup>Mechanical Engineering, KAIST, Yuseong-gu, Daejeon 34141, Republic of Korea.

6    <sup>3</sup>Mechanical Engineering, Stanford University, Stanford, CA 94305, USA.

7    <sup>4</sup>Advanced Light Source, Lawrence Berkeley National Lab, Berkeley 94720, USA.

8

9    **Abstract:** Nanocrystals can exist in multiply twinned structures like icosahedron, or single  
10    crystalline structures like cuboctahedron. Transformations between these structures can proceed  
11    through diffusion or displacive motion. Experimental studies on nanocrystal structural  
12    transformations have focused on high temperature diffusion mediated processes. Limited  
13    experimental evidence of displacive motion exists. We report structural transformation of 6 nm  
14    Au nanocrystals under nonhydrostatic pressure of 7.7 GPa in a diamond anvil cell that is driven  
15    by displacive motion. X-ray diffraction and transmission electron microscopy were used to detect  
16    the structural transformation from multiply twinned to single crystalline. Single crystalline  
17    nanocrystals were recovered after unloading, then quickly reverted to the multiply twinned state  
18    after dispersion in toluene. The dynamics of recovery was captured using TEM which showed  
19    surface recrystallization and rapid twin boundary motion. Molecular dynamics simulations showed  
20    that twin boundaries are unstable due to defects nucleated from the interior of the nanocrystal.

21

22    **Keywords:** Diamond Anvil Cell, X-ray Diffraction, Transmission Electron Microscopy  
23    Molecular Dynamics Simulation, Asymmetric Mackay-like Transformation

24 **Main Text:**

25 Metallic nanocrystals are used widely in fields such as photonics, biomedical therapies, catalysis,  
26 electronics and sensing<sup>1</sup>. Properties of these nanocrystals are highly dependent on their size, shape,  
27 and crystalline structure<sup>2</sup>. Multiply twinned (MT) icosahedron, MT decahedron, single-crystal  
28 (SC) cuboctahedron, and SC Wulff-polyhedron nanocrystal shapes are commonly observed, and  
29 can have different catalytic, magnetic, mechanical, structural, and electronic properties<sup>3-8</sup>. For this  
30 reason, it is often desirable to synthesize one particular nanocrystal size and shape, and maintain  
31 this structure during use. This remains difficult because the thermodynamic stability and structural  
32 transitions between different nanocrystal structures are still incompletely understood. The  
33 structural transformation of polyhedral structures such as MT icosahedron is also important for  
34 understanding materials like metallic glasses and magnetic nanoclusters, in which polyhedral  
35 atomic clusters make up the basic structural unit, and changes in these atomic clusters dictate  
36 material properties<sup>9-11</sup>.

37 Structural transformation between different nanocrystal shapes have been studied using  
38 theory, simulations, and experiments. Using energy balance calculations and molecular dynamics  
39 (MD) simulations that consider differences in surface energy and lattice strain, it has been  
40 determined that MT nanocrystals are stable at smaller sizes and SC nanocrystals are stable at larger  
41 sizes<sup>9,12-14</sup>. The transition occurs from 2 to 10 nm depending on the calculation method, and varies  
42 in experiments due to the influence of surface ligands, solvents and substrates on surface energy.  
43 It has been proposed that the transformation between MT and SC structures occurs through  
44 diffusive or displacive processes, such as surface melting and restructuring,  
45 dislocation/disclination activity, and the symmetric and asymmetric Mackay-like transformation<sup>15-</sup>  
46 <sup>19</sup>. Transformation in nanocrystals have been studied experimentally by heating nanocrystals with

47 the electron beam in a transmission electron microscope (TEM), high energy laser pulses, and  
48 annealing nanocrystals on a substrate<sup>16,17,20-23</sup>. These experimental studies observed that enhanced  
49 mobility, melting and recrystallization of nanocrystals lead to diffusion mediated structural  
50 transformations. However, displacive motion mediated structural transformation has not been  
51 studied systematically in nanocrystals.

52 High-pressure compression in a diamond anvil cell (DAC) is an ideal technique to study  
53 displacive motion in nanomaterials, because diffusion is suppressed at high pressure<sup>24</sup>. DAC has  
54 previously been used to study high-pressure phase transformation, crystallization and sintering of  
55 aggregated nanocrystals<sup>25</sup>. DAC techniques have also been used to study structural transformations  
56 in Ag nanocrystals under hydrostatic pressures,<sup>26</sup> which minimizes both diffusion and displacive  
57 motion. Here, we study the structural stability and structural transformation between MT and SC  
58 nanocrystals by compressing 6 nm Au nanocrystals in a DAC under non-hydrostatic pressure, and  
59 monitoring nanocrystal structure using *in situ* X-ray diffraction (XRD). The nanocrystals are  
60 recovered after compression and imaged using TEM. We find that the 6 nm nanocrystals undergo  
61 a MT to SC transformation after compression to 7.7 GPa of pressure. This is in contrast to smaller,  
62 3.9 nm Au nanocrystals which did not show a structural transformation under pressure, and instead  
63 formed stacking faults via surface nucleated partial dislocations<sup>27</sup>. MD simulations were conducted  
64 to understand defect formation in nanocrystals of 3.9 nm and 6 nm in size. These simulations  
65 showed that dislocation activity is enhanced in larger nanocrystals. These results indicate that  
66 displacive motion driven large scale structural transformation is possible in nanocrystals and must  
67 be considered in designing structures at the nanoscale.

68

69 MT Au nanocrystals were synthesized using organic phase reduction of chloroauric acid  
70 and capped with dodecanethiol ligands<sup>28</sup>. The nanocrystal size distribution was found to be  $6.0 \pm 0.3$   
71 nm using TEM (see Fig. 1A and Fig. S1). High-resolution TEM images showed that the majority  
72 of nanocrystals (~80%) were MT and remaining nanocrystals were SC (a total of 59 nanocrystals  
73 were analyzed). The MT nanocrystals were icosahedral structures which are formed with 20  
74 tetrahedral units joined by 20 twin boundaries. An icosahedral polyhedron has 6 5-fold, 10 3-fold,  
75 and 15 2-fold axes. Fig. 1B shows the icosahedral nanocrystal along the 3-fold axis and Fig. 1C  
76 shows the icosahedral nanocrystal along a 2-fold axis. The SC nanocrystals were cuboctahedron  
77 or Wulff-polyhedron in structure, and sometimes contained 1-2 twin boundaries rather than the  
78 high density of twin boundaries in MT nanocrystals.

79 Ambient pressure XRD for the nanocrystals showed an FCC crystal structure, and  
80 significantly broader peaks than bulk Au due to crystallite size broadening (see Fig. S2).  
81 Nanocrystal surfaces exert a Laplace pressure on the interior of the nanocrystal, which scales  
82 inversely with the radius<sup>29</sup>. This compressive force shifts all the ambient pressure XRD peaks  
83 except the (200) peak to a higher  $2\theta$  angle compared to the bulk. The {111} planes form the surface  
84 of MT icosahedral nanocrystals. Hence, the (111) peak was shifted by  $\sim 0.06^\circ 2\theta$  compared to the  
85 bulk, which corresponds to a volumetric strain of  $\sim 1.5\%$ . The position of the (200) peak does not  
86 shift in the same way as the other peaks because it is affected by twinning in the nanocrystal. This  
87 was previously shown in a model which revealed that the (200) peak shifts towards lower  $2\theta$  angles  
88 with an increase in twinning density<sup>30,31</sup>. This model simulates the effect of low twinning density  
89 and cannot be directly applied to MT nanocrystals which each contain 20 twins, but the qualitative  
90 trend is still relevant. Another feature of the (200) peak is the double peak which is due to the  
91 mixture of 80% MT and 20% SC nanocrystals. One peak is located at the bulk (200) peak position,

92 and the other is shifted towards lower  $2\theta$  angles by  $\sim 0.6^0$   $2\theta$ . The icosahedral nanocrystals  
93 correspond to the lower  $2\theta$  (200) peak, which is shifted due to the twins, and the SC nanocrystals  
94 correspond to the (200) peak at the bulk position.

95 High-pressure XRD was obtained *in situ* during DAC compression experiments at the  
96 Advanced Light Source at Lawrence Berkeley National Laboratory. Toluene was used as the  
97 pressure medium and toluene becomes non-hydrostatic above 1.9 GPa pressure<sup>32</sup>. The nanocrystals  
98 were loaded as a thick film at the bottom of the DAC sample chamber. XRD was collected while  
99 the nanocrystals were loaded up to 7.7 GPa and as pressure was released. The pressure was limited  
100 to 7.7 GPa to avoid sintering between the nanocrystals, which has been observed at higher  
101 pressures<sup>33-35</sup>. The XRD peak position and width (full width at half maximum) were observed to  
102 change with increasing and decreasing pressure and were quantified at each pressure (Fig. 2).

103 High-pressure XRD and the corresponding peak positions and widths are shown in Fig. 2.  
104 The shift in XRD peak position indicates the pressure-induced elastic strain in the nanocrystals.  
105 XRD peak position for all peaks except the (200) peak recovered completely with pressure cycling  
106 to within 0.1% of their original value (Fig. 2 D). An irreversible change was observed for the (200)  
107 peak position with pressure cycling (Fig. 2 B). The ratio of the left to the right (200) peak intensities  
108 is proportional to the degree of twinning, or the fraction of MT to SC nanocrystals in the sample<sup>30</sup>.  
109 After pressure cycling, this ratio decreased by  $\sim 22\%$ : the right (200) peak intensity increased  
110 significantly with pressure and remained at higher values after unloading, while the left (200) peak  
111 decreased in intensity. This indicated that the MT nanocrystals detwinned with pressure cycling  
112 and underwent a structural transformation from MT to SC. Changes in peak width with pressure  
113 cycling also indicate that this structural transformation occurred (see Fig. 2 C). The XRD peak

114 width for (111), (220) and (311) peaks decreased by 11%, 19%, and 22%, respectively. This can  
115 be explained by an increase in crystallite size upon transformation from MT to SC nanocrystals<sup>36</sup>.

116 Post-compression TEM imaging corroborated these findings. Nanocrystals were loaded to  
117 ~5 GPa in the DAC. The sample was then quickly unloaded, and the sample chamber was opened  
118 to air to dry out the liquid toluene. The nanocrystals were picked up using a needle and scraped  
119 onto a TEM grid and inserted into the TEM within 10 minutes. The post-compression TEM images  
120 are shown in Fig. 3. We found that the ratio of nanocrystals changed from 80% MT and 20% SC  
121 nanocrystals before pressure cycling, to 40% MT and 60% SC nanocrystals after pressure cycling.

122 The fraction of MT nanocrystals decreased by 50% with pressure cycling. High-resolution TEM  
123 images of 59 as-synthesized and 23 post-compression nanocrystals were analyzed. Post-  
124 compression nanocrystals were SC with cuboctahedron, truncated-octahedron or Wulff-  
125 polyhedron shapes (Fig. 3). Some SC nanocrystals had a twin that extended across the nanocrystal  
126 (Fig. 3 B). Using the ratio of MT to SC nanocrystals from TEM, the Debye scattering equation  
127 was used to simulate pre- and post-compression XRD patterns. Fig. S4 shows the simulated XRD  
128 pattern for mixtures of 80:20 and 40:60 MT and SC nanocrystals. The simulated XRD pattern  
129 showed similar trends as the experimental XRD patterns, in which the ratio of the left and right  
130 (200) peaks decreased with decreasing fraction of MT nanocrystals. This showed that the post-  
131 compression TEM analysis matches the high-pressure XRD patterns.

132 The post-compression SC structure of the nanocrystal was observed to be unstable. Toluene  
133 was added drop by drop to a TEM grid with post-compression nanocrystals. TEM imaging was  
134 performed after waiting for 10-15 mins, which showed that the ratio of MT to SC structures  
135 reverted close to the as-synthesized value (85% MT and 15% SC, 48 nanocrystals analyzed). This  
136 showed that the nanocrystal can rapidly convert to the thermodynamically stable MT structure in

137 solution at ambient pressure (see Fig. S5). The dynamics and mobility of twin boundaries in  
138 nanocrystals was further investigated by heating individual nanocrystals under a 200 keV electron  
139 beam within the TEM. TEM movie and snapshots of the nanocrystal coalescence process<sup>37-40</sup> is  
140 shown in Supplementary Movie S1 and Fig. 4. At the start of the movie, nanocrystal I is 7 nm in  
141 size and has two visible inclined twin boundaries at 35°. Nanocrystal II is 6.3 nm in size and has a  
142 MT structure (Fig. 4 A). Fig. 4 B, C and D show the nanocrystals after 10 s, 40 s and 70 s of  
143 electron beam irradiation, respectively. After 10 s, nanocrystal I rapidly developed a MT structure  
144 in the lower half of the nanocrystal, and the angle between the twin boundaries increased to ~70°.  
145 The surface of nanocrystal I started melting and sintering with the nanocrystal II. After 40 s, the  
146 surface of nanocrystal II started melting and nanocrystal II rotated to sinter with the nanocrystal I.  
147 The twin boundaries in nanocrystal I dynamically moved away from the sintered part of the  
148 nanocrystal. Fig. 4 D shows final state of the nanocrystals. A SC region connects both nanocrystals.  
149 The nanocrystal I has a MT structure with the twin boundaries at an angle of ~71° which is close  
150 to the ideal ~72° for a strained penta-twinned structure. This showed that the twin boundaries in  
151 nanocrystal can evolve due to enhanced diffusion under excitation by the electron beam. It is likely  
152 that the enhanced mobility of twin boundaries and interaction of ligands/surface of the nanocrystal  
153 with toluene solvent resulted in the rapid recovery of MT structure from SC nanocrystal in solution.  
154 The post-compression TEM and high-pressure XRD analysis confirmed that the MT 6 nm  
155 nanocrystals transformed into SC nanocrystals with pressure cycling, and the SC structure was  
156 unstable at ambient pressure and reverted back to MT structure after leaving in solution for short  
157 time.

158 The high-pressure behavior of 6 nm nanocrystals differs from that of 3.9 nm nanocrystals  
159 previously studied by our group<sup>27</sup>. High pressure experiments for 3.9 nm nanocrystals showed that

160 all the XRD peak positions including the (200) peak recovered with pressure cycling to within  
161 0.2% of its original value (see Fig. S6). The complete recovery of the (200) peak position indicated  
162 that the MT structure of the 3.9 nm nanocrystal was preserved with pressure cycling. In addition,  
163 the XRD peak widths for 3.9 nm nanocrystals showed the opposite trend as for 6 nm nanocrystals.  
164 The 3.9 nm XRD peak widths for (200) and (220) peaks increased by 16% and 23%, respectively,  
165 and remained at higher values after unloading. The peak width for (111) plane remained at about  
166 2% of its initial value with pressure cycling. This indicated the introduction of surface nucleated  
167 partial dislocations (stacking faults) with pressure cycling.

168 The size-dependent MT to SC structural transformation can be analyzed in terms of the  
169 thermodynamic stability of the two structures. Howie and Marks represented the energy of a  
170 nanocrystal as:<sup>41</sup>

$$U = W_s + W_\gamma + W_{el} + H(V) \quad (1)$$

171 Where  $W_s$ ,  $W_\gamma$ ,  $W_{el}$  and  $H(V)$  are the energy due to surface stress, energy due to strain in the  
172 surface, elastic strain energy due to applied external pressure and nanocrystal geometry, and  
173 cohesive energy, respectively. Using this approach, it is found that the MT structure is stable at  
174 smaller sizes, the SC structure is stable at larger sizes and that the MT structure transforms into  
175 SC structure at a critical nanocrystal size of 7.2 nm at ambient pressure. At high pressure, the  
176 elastic strain energy and energy due to strain in the surface is modified to include additional energy  
177 input from the external pressure (see supplementary information). The transition size reduces with  
178 increasing pressure (see Fig. S7) and is 5.4 nm at 7.7 GPa (the maximum applied pressure in the  
179 experiments). This shows that it is thermodynamically favorable for 6 nm nanocrystals to be SC  
180 at high pressure, while it is favorable for 3.9 nm nanocrystals to be MT.

181         Similarly, MD simulations have shown that the MT structure is stable at smaller sizes and  
182         the SC structure is stable at larger sizes<sup>9,13,14,42</sup>. The MT structure transforms into the SC structure  
183         at a critical nanocrystal size of ~2-5 nm depending on the interatomic potential. This transition  
184         reflects the lower surface energy and higher lattice strain of MT structures. At high pressures, the  
185         MT structure is unfavorable compared to the SC structure due to its lower atomic packing  
186         fraction<sup>19</sup>.

187         Next, we consider the atomistic mechanism of the MT to SC transition at high pressure.  
188         Transformations in nanocrystals can occur through surface diffusion mediated mechanisms at  
189         elevated temperatures<sup>21,22</sup>. Diffusion is suppressed at high pressure and cannot be the mechanism  
190         for the MT to SC transformation in the nanocrystals<sup>24</sup>. At high pressure, the transformation can  
191         occur through a nondiffusive Mackay transformation or a dislocation/disclination mediated  
192         detwinning process. The Mackay transformation is displacive atomic motion driven MT  
193         icosahedron to SC cuboctahedron transformation which can proceed through symmetric<sup>19</sup> or  
194         asymmetric paths<sup>15</sup> (Fig. S8). The Mackay transformation requires low activation energy<sup>43-45</sup>.  
195         Simulation studies predict the dynamics of transformation using total energy calculation along the  
196         Mackay path<sup>15,43,46,47</sup> or MD simulations for small nanocrystals<sup>48-50</sup>. Symmetric Mackay  
197         transformation is not compatible with deviatoric stresses however, the asymmetric Mackay-like  
198         transformation can be driven by deviatoric stresses. The MT to SC structural transformation can  
199         also proceed through dislocation or disclination mediated detwinning. Dislocation mediated  
200         detwinning was previously observed in large Pt nanocrystal under oxidative heating<sup>17</sup>. The SC  
201         grain nucleated at the surface of the nanocrystal and then grew when dislocation motion led to the  
202         retraction of twin boundaries. This transformation has also been observed to occur through the  
203         motion of disclinations<sup>18</sup>.

204 The MT to SC transition is driven by deviatoric stresses caused by the nonhydrostatic  
 205 pressure medium. The stress in the nanocrystals is higher along the loading axis (and the direction  
 206 of imaging) than in the transverse direction. The difference between axial and transverse stress is  
 207 termed differential stress. Differential stress in the sample chamber can be estimated using the  
 208 lattice strain theory for FCC metals<sup>51</sup>. The maximum differential stress in 6 nm nanocrystals was  
 209 ~2 GPa (see Fig. S9). We have previously shown that 3.9 nm nanocrystals can sustain dislocation  
 210 activity due to the deviatoric stresses, while sustaining its twin boundary structures<sup>27</sup>. In order to  
 211 understand the size-dependent stability of twin boundary structures, we performed MD simulations  
 212 of 3.9 nm and 6 nm icosahedral nanocrystals (Fig. 5). Although the direct observation of structural  
 213 transformation was not accessible in MD simulation due to the limited timescale, we were able to  
 214 quantify the size-dependent pre-stress and to discover different twin boundary stabilities in small  
 215 and large nanocrystals. While the angle between two non-parallel {111} surfaces is 70.53° in bulk  
 216 FCC crystals, the twin boundaries in icosahedral nanocrystals form a 72° angle due to the five-  
 217 fold symmetry, which inevitably induces pre-stress from the mismatch strain. The mismatch strain  
 218 and resulting pre-stress inside icosahedral and decahedral MT nanocrystals can be approximated  
 219 by the superposition of multiple finite-length disclinations. By assuming elastic isotropy and  
 220 spherical surface, the pre-stress distribution inside MT icosahedral nanocrystal can be  
 221 approximated as follows (see supplementary information).

$$\sigma_{rr} = \frac{4\mu\epsilon_I}{3} \left( \frac{1+\nu}{1-\nu} \right) \ln \left( \frac{r}{R} \right) - P \quad (2)$$

222 where  $\epsilon_I = 0.0615$ ,  $\mu$  is the shear modulus,  $\nu$  is the Poisson's ratio,  $R$  is the radius of the  
 223 nanocrystal,  $P$  is the external pressure, and  $r, \theta$  and  $\phi$  are the spherical coordinates. The solution  
 224 indicates pure compressive stress along the radial direction. The maximum value of compressive  
 225 stress is found to be higher in the larger nanocrystal. Smaller nanocrystals are subjected to higher

226 average strain energy and larger hydrostatic compression due to higher Laplace pressure from  
227 surface stress<sup>41</sup>. This is consistent with our ambient pressure XRD measurement where 3.9 nm  
228 shows a larger shift in the (111) peak position. Even though the theoretical analysis omits elastic  
229 anisotropy, the analytical solution with  $\ln \frac{r}{R}$  dependence matches qualitatively well with the atomic  
230 potential energy distribution depicted in Fig. 5 B, which shows that 3.9 and 6 nm nanocrystals  
231 have higher strain energy density near the core and 6 nm nanocrystal has larger maximum atomic  
232 potential energy (i.e. higher pre-stress). Defect nucleation from the pristine twin structure is likely  
233 to initiate from the region of high pre-stress, so it is expected that defect nucleation occurs  
234 preferentially near the core of the MT nanocrystal. The MT structure in the larger nanocrystal is  
235 more susceptible to defect nucleation near the core because of its higher maximum pre-stress and  
236 can sustain pre-existing dislocations at ambient pressure. The twin boundary structures with five-  
237 fold symmetry become progressively unstable for larger MT nanocrystals. We found that, even in  
238 the absence of any external stimuli, dislocation nucleation and distortion of twin boundaries were  
239 observed in 6 nm icosahedral nanocrystal in vacuum under relatively long high temperature MD  
240 simulation, while neither dislocation activity nor distortion of twin boundary structure is observed  
241 in the 3.9 nm nanocrystal due to smaller pre-stress (Fig. 5 C). These unstable twin boundary  
242 structures and pre-existing defects allow deviatoric stress on the 6 nm MT nanocrystal to drive the  
243 asymmetric Mackay-like transformation or dislocation/disclination mediated detwinning.

244 In summary, we have used high-pressure XRD and post-compression TEM to provide the  
245 first evidence of deviatoric stress induced MT to SC structural transformation in nanocrystals.  
246 Energy calculations showed that the 6 nm MT nanocrystals become unstable at high pressures and  
247 the critical size for transition between MT and SC nanocrystals reduces with increasing pressure.  
248 MD simulations showed that the 6 nm MT nanocrystal was more susceptible to dislocation

249 nucleation, had unstable twin boundaries and can have pre-existing dislocations. Deviatoric stress  
250 driven kinetics of the process is governed by two possible paths – asymmetric Mackay-like  
251 transformation or dislocation/disclination mediated detwinning. High-pressure SC nanocrystals  
252 were recovered after unloading, however, the nanocrystals quickly reverted back to MT state after  
253 redispersion in toluene solvent. The *in situ* TEM heating experiment indicated that the recovery  
254 can be governed by surface recrystallization, and rapid nucleation and motion of twin boundaries.  
255

256 ASSOCIATED CONTENT

257 **Supporting Information.**

258 The Supporting information is available free of charge on the ACS Publication website at DOI:

259 • Detailed methods and experimental conditions with additional figures detailing data  
260 analysis, nanocrystal size distribution, simulated XRD patterns, TEM images,  
261 calculations for deviatoric stress and bulk modulus, derivation of thermodynamic MT to  
262 SC transition under pressure (PDF)

263 • TEM heating movie showing the nanocrystal twin boundary motion (MP4)

264

265 AUTHOR INFORMATION

266 **Corresponding Author**

267 \*Corresponding author:

268 X. Wendy Gu

269 452 Escondido Mall, Room 227,

270 Stanford University, Stanford CA 94305

271 650-497-3189

272 [xwgu@stanford.edu](mailto:xwgu@stanford.edu)

273 **Author Contributions**

274 X.W.G. and A.P. conceived the idea and X.W.G. supervised the research of this work. A.P.  
275 synthesized the nanocrystals and M.T.K performed the TEM characterization. A.P., M.T.K., D.D.,  
276 M.K. and A.D. performed the high-pressure XRD. A.P. performed the XRD simulation and  
277 analysis. S.L. and S.R. performed the MD simulations and analysis. A.P., S.L., S.R. and X.W.G.  
278 wrote the manuscript. All authors have given approval to the final version of the manuscript.

279 **Notes**

280 Authors declare no competing financial interest.

281

282 **ACKNOWLEDGMENT**

283 X.W.G. and A.P. acknowledge financial support from the National Science Foundation under  
284 Grant No. DMR-2002936/2002891. The Advanced Light Source is supported by the Director,  
285 Office of Science, Office of Basic Energy Sciences, of the U.S. Department of Energy under  
286 Contract No. DE-AC02-05CH11231. Beamline 12.2.2 is partially supported by COMPRES, the  
287 Consortium for Materials Properties Research in Earth Sciences under NSF Cooperative  
288 Agreement EAR 1606856. Part of this work was performed at the Stanford Nano Shared Facilities  
289 (SNSF), supported by the National Science Foundation under award ECCS-1542152. M.T.K. is  
290 supported by the National Defense and Science Engineering Graduate Fellowship. D.D. is  
291 supported by the NSF Graduate Fellowship. S.L. and S.R. are supported by the Creative Materials  
292 Discovery Program (2016M3D1A1900038) through the National Research Foundation of Korea  
293 (NRF) funded by the Ministry of Science and ICT.

294

295 **ABBREVIATIONS**

296 XRD, X-ray Diffraction; DAC, diamond anvil cell; MD, molecular dynamics; TEM,  
297 transmission electron microscopy; SC, single crystalline; MT, multiply twinned.

298

299 REFERENCES

300 (1) Xia, Y.; Xiong, Y.; Lim, B.; Skrabalak, S. E. Shape-Controlled Synthesis of Metal  
301 Nanocrystals: Simple Chemistry Meets Complex Physics? *Angewandte Chemie -*  
302 *International Edition*. John Wiley & Sons, Ltd January 1, 2009, pp 60–103.  
303 <https://doi.org/10.1002/anie.200802248>.

304 (2) Burda, C.; Chen, X.; Narayanan, R.; El-Sayed, M. A. Chemistry and Properties of  
305 Nanocrystals of Different Shapes. *Chemical Reviews*. 2005, pp 1025–1102.  
306 <https://doi.org/10.1021/cr030063a>.

307 (3) Goubet, N.; Yan, C.; Polli, D.; Portalès, H.; Arfaoui, I.; Cerullo, G.; Pileni, M. P.  
308 Modulating Physical Properties of Isolated and Self-Assembled Nanocrystals through  
309 Change in Nanocrystallinity. *Nano Lett.* **2013**, *13* (2), 504–508.  
310 <https://doi.org/10.1021/nl303898y>.

311 (4) Uttam, P.; Kumar, V.; Kim, K. H.; Deep, A. Nanotwinning: Generation, Properties, and  
312 Application. *Materials and Design*. Elsevier Ltd July 1, 2020, p 108752.  
313 <https://doi.org/10.1016/j.matdes.2020.108752>.

314 (5) Tang, Y.; Ouyang, M. Tailoring Properties and Functionalities of Metal Nanoparticles  
315 through Crystallinity Engineering. *Nat. Mater.* **2007**, *6* (10), 754–759.  
316 <https://doi.org/10.1038/nmat1982>.

317 (6) Huang, H.; Jia, H.; Liu, Z.; Gao, P.; Zhao, J.; Luo, Z.; Yang, J.; Zeng, J. Understanding of  
318 Strain Effects in the Electrochemical Reduction of CO<sub>2</sub>: Using Pd Nanostructures as an  
319 Ideal Platform. *Angew. Chemie - Int. Ed.* **2017**, *56* (13), 3594–3598.  
320 <https://doi.org/10.1002/anie.201612617>.

321 (7) Wang, X.; Choi, S. Il; Roling, L. T.; Luo, M.; Ma, C.; Zhang, L.; Chi, M.; Liu, J.; Xie, Z.;

322 Herron, J. A.; Mavrikakis, M.; Xia, Y. Palladium-Platinum Core-Shell Icosahedra with  
323 Substantially Enhanced Activity and Durability towards Oxygen Reduction. *Nat.*  
324 *Commun.* **2015**, *6* (1), 1–8. <https://doi.org/10.1038/ncomms8594>.

325 (8) Xia, Y.; Gilroy, K. D.; Peng, H. C.; Xia, X. Seed-Mediated Growth of Colloidal Metal  
326 Nanocrystals. *Angewandte Chemie - International Edition*. Wiley-VCH Verlag January 2,  
327 2017, pp 60–95. <https://doi.org/10.1002/anie.201604731>.

328 (9) Baletto, F.; Ferrando, R. Structural Properties of Nanoclusters: Energetic,  
329 Thermodynamic, and Kinetic Effects. *Rev. Mod. Phys.* **2005**, *77* (1), 371–423.  
330 <https://doi.org/10.1103/RevModPhys.77.371>.

331 (10) Gruner, M. E.; Entel, P. Simulating Functional Magnetic Materials on Supercomputers. *J.*  
332 *Phys. Condens. Matter* **2009**, *21* (29), 31. <https://doi.org/10.1088/0953-8984/21/29/293201>.

334 (11) Sheng, H. W.; Luo, W. K.; Alamgir, F. M.; Bai, J. M.; Ma, E. Atomic Packing and Short-  
335 to-Medium-Range Order in Metallic Glasses. *Nature* **2006**, *439* (7075), 419–425.  
336 <https://doi.org/10.1038/nature04421>.

337 (12) Ino, S. Stability of Multiply-Twinned Particles. *J. Phys. Soc. Japan* **1969**, *27* (4), 941–  
338 953. <https://doi.org/10.1143/JPSJ.27.941>.

339 (13) Baletto, F.; Ferrando, R.; Fortunelli, A.; Montalenti, F.; Mottet, C. Crossover among  
340 Structural Motifs in Transition and Noble-Metal Clusters. *J. Chem. Phys.* **2002**, *116* (9),  
341 3856–3863. <https://doi.org/10.1063/1.1448484>.

342 (14) Myshlyavtsev, A. V.; Stishenko, P. V.; Svalova, A. I. A Systematic Computational Study  
343 of the Structure Crossover and Coordination Number Distribution of Metallic  
344 Nanoparticles. *Phys. Chem. Chem. Phys.* **2017**, *19* (27), 17895–17903.

345 https://doi.org/10.1039/c6cp07571a.

346 (15) Plessow, P. N. The Transformation of Cuboctahedral to Icosahedral Nanoparticles:  
347      Atomic Structure and Dynamics. *Phys. Chem. Chem. Phys.* **2020**, *22* (23), 12939–12945.  
348 https://doi.org/10.1039/d0cp01651a.

349 (16) Vogel, W.; Bradley, J.; Vollmer, O.; Abraham, I. Transition from Five-Fold Symmetric to  
350      Twinned FCC Gold Particles by Thermally Induced Growth. *J. Phys. Chem. B* **1998**, *102*  
351      (52), 10853–10859. https://doi.org/10.1021/jp9827274.

352 (17) Gao, W.; Wu, J.; Yoon, A.; Lu, P.; Qi, L.; Wen, J.; Miller, D. J.; Mabon, J. C.; Wilson, W.  
353      L.; Yang, H.; Zuo, J. M. Dynamics of Transformation from Platinum Icosahedral  
354      Nanoparticles to Larger FCC Crystal at Millisecond Time Resolution. *Sci. Rep.* **2017**, *7*  
355      (1). https://doi.org/10.1038/s41598-017-16900-6.

356 (18) Ajayan, P. M.; Marks, L. D. Phase Instabilities in Small Particles. *Phase Transitions A  
357      Multinatl. J.* **1990**, *1*, 229–258. https://doi.org/10.1080/01411599008210232.

358 (19) Mackay, A. L. A Dense Non-Crystallographic Packing of Equal Spheres. *Acta  
359      Crystallogr.* **1962**, *15* (9), 916–918. https://doi.org/10.1107/s0365110x6200239x.

360 (20) Inasawa, S.; Sugiyama, M.; Yamaguchi, Y. Laser-Induced Shape Transformation of Gold  
361      Nanoparticles below the Melting Point: The Effect of Surface Melting. *J. Phys. Chem. B*  
362      **2005**, *109* (8), 3104–3111. https://doi.org/10.1021/jp045167j.

363 (21) Bovin, J. O.; Malm, J. O. Atomic Resolution Electron Microscopy of Small Metal  
364      Clusters. *Zeitschrift für Phys. D Atoms, Mol. Clust.* **1991**, *19* (4), 293–298.  
365 https://doi.org/10.1007/BF01448314.

366 (22) Iijima, S.; Ichihashi, T. Structural Instability of Ultrafine Particles of Metals. *Phys. Rev.  
367      Lett.* **1986**, *56* (6), 616–619. https://doi.org/10.1103/PhysRevLett.56.616.

368 (23) Gilroy, K. D.; Puibasset, J.; Vara, M.; Xia, Y. On the Thermodynamics and Experimental  
369 Control of Twinning in Metal Nanocrystals. *Angew. Chemie - Int. Ed.* **2017**, *56* (30),  
370 8647–8651. <https://doi.org/10.1002/anie.201705443>.

371 (24) Dobson, D. P. Self-Diffusion in Liquid Fe at High Pressure. *Phys. Earth Planet. Inter.*  
372 **2002**, *130* (3–4), 271–284. [https://doi.org/10.1016/S0031-9201\(02\)00011-0](https://doi.org/10.1016/S0031-9201(02)00011-0).

373 (25) Bai, F.; Bian, K.; Huang, X.; Wang, Z.; Fan, H. Pressure Induced Nanoparticle Phase  
374 Behavior, Property, and Applications. *Chemical Reviews*. American Chemical Society  
375 June 26, 2019, pp 7673–7717. <https://doi.org/10.1021/acs.chemrev.9b00023>.

376 (26) Koski, K. J.; Kamp, N. M.; Smith, R. K.; Kunz, M.; Knight, J. K.; Alivisatos, A. P.  
377 Structural Distortions in 5-10 Nm Silver Nanoparticles under High Pressure. *Phys. Rev. B*  
378 - *Condens. Matter Mater. Phys.* **2008**, *78* (16), 165410.  
379 <https://doi.org/10.1103/PhysRevB.78.165410>.

380 (27) Parakh, A.; Lee, S.; Harkins, K. A.; Kiani, M. T.; Doan, D.; Kunz, M.; Doran, A.; Hanson,  
381 L. A.; Ryu, S.; Gu, X. W. Nucleation of Dislocations in 3.9 Nm Nanocrystals at High  
382 Pressure. *Phys. Rev. Lett.* **2020**, *124* (10), 106104.  
383 <https://doi.org/10.1103/PhysRevLett.124.106104>.

384 (28) Peng, S.; Lee, Y.; Wang, C.; Yin, H.; Dai, S.; Sun, S. A Facile Synthesis of Monodisperse  
385 Au Nanoparticles and Their Catalysis of CO Oxidation. *Nano Res.* **2008**, *1* (3), 229–234.  
386 <https://doi.org/10.1007/s12274-008-8026-3>.

387 (29) Jiang, Q.; Liang, L. H.; Zhao, D. S. Lattice Contraction and Surface Stress of Fcc  
388 Nanocrystals. *J. Phys. Chem. B* **2001**, *105* (27), 6275–6277.  
389 <https://doi.org/10.1021/jp010995n>.

390 (30) Longo, A.; Martorana, A. Distorted f.c.c. Arrangement of Gold Nanoclusters: A Model of

391 Spherical Particles with Microstrains and Stacking Faults. *J. Appl. Crystallogr.* **2008**, *41*  
392 (2), 446–455. <https://doi.org/10.1107/S0021889808004846>.

393 (31) Warren, B. E. X-Ray Measurement of Stacking Fault Widths in Fcc Metals. *J. Appl. Phys.*  
394 **1961**, *32* (11), 2428–2431. <https://doi.org/10.1063/1.1777086>.

395 (32) Herbst, C. .; Cook, R. .; King, H. . Density-Mediated Transport and the Glass Transition:  
396 High Pressure Viscosity Measurements in the Diamond Anvil Cell. *J. Non. Cryst. Solids*  
397 **1994**, *172–174*, 265–271. [https://doi.org/10.1016/0022-3093\(94\)90445-6](https://doi.org/10.1016/0022-3093(94)90445-6).

398 (33) Li, B.; Wen, X.; Li, R.; Wang, Z.; Clem, P. G.; Fan, H. Stress-Induced Phase  
399 Transformation and Optical Coupling of Silver Nanoparticle Superlattices into  
400 Mechanically Stable Nanowires. *Nat. Commun.* **2014**, *5* (1), 4179.  
401 <https://doi.org/10.1038/ncomms5179>.

402 (34) Wang, Z.; Schliehe, C.; Wang, T.; Nagaoka, Y.; Cao, Y. C.; Bassett, W. A.; Wu, H.; Fan,  
403 H.; Weller, H. Deviatoric Stress Driven Formation of Large Single-Crystal PbS Nanosheet  
404 from Nanoparticles and in Situ Monitoring of Oriented Attachment. *J. Am. Chem. Soc.*  
405 **2011**, *133* (37), 14484–14487. <https://doi.org/10.1021/ja204310b>.

406 (35) Li, B.; Bian, K.; Lane, J. M. D.; Salerno, K. M.; Grest, G. S.; Ao, T.; Hickman, R.; Wise,  
407 J.; Wang, Z.; Fan, H. Superfast Assembly and Synthesis of Gold Nanostructures Using  
408 Nanosecond Low-Temperature Compression via Magnetic Pulsed Power. *Nat. Commun.*  
409 **2017**, *8*, 14778.

410 (36) Cullity, B. D.; Stock, S. R. *Elements of X-Ray Diffraction*; 2014.

411 (37) Song, M.; Zhou, G.; Lu, N.; Lee, J.; Nakouzi, E.; Wang, H.; Li, D. Oriented Attachment  
412 Induces Fivefold Twins by Forming and Decomposing High-Energy Grain Boundaries.  
413 *Science (80-.)*. **2020**, *367* (6473), 40–45. <https://doi.org/10.1126/science.aax6511>.

414 (38) Lim, T. H.; McCarthy, D.; Hendy, S. C.; Stevens, K. J.; Brown, S. A.; Tilley, R. D. Real-  
415 Time TEM and Kinetic Monte Carlo Studies of the Coalescence of Decahedral Gold  
416 Nanoparticles. *ACS Nano* **2009**, *3* (11), 3809–3813. <https://doi.org/10.1021/nn9012252>.

417 (39) José-Yacamán, M.; Gutierrez-Wing, C.; Miki, M.; Yang, D. Q.; Piyakis, K. N.; Sacher, E.  
418 Surface Diffusion and Coalescence of Mobile Metal Nanoparticles. *J. Phys. Chem. B*  
419 **2005**, *109* (19), 9703–9711. <https://doi.org/10.1021/jp0509459>.

420 (40) Chen, Y.; Palmer, R. E.; Wilcoxon, J. P. Sintering of Passivated Gold Nanoparticles under  
421 the Electron Beam. *Langmuir* **2006**, *22* (6), 2851–2855.  
422 <https://doi.org/10.1021/la0533157>.

423 (41) Howie, A.; Marks, L. D. Elastic Strains and the Energy Balance for Multiply Twinned  
424 Particles. *Philos. Mag. A Phys. Condens. Matter, Struct. Defects Mech. Prop.* **1984**, *49*  
425 (1), 95–109. <https://doi.org/10.1080/01418618408233432>.

426 (42) Wang, Y.; Teitel, S.; Dellago, C. Melting of Icosahedral Gold Nanoclusters from  
427 Molecular Dynamics Simulations. *J. Chem. Phys.* **2005**, *122* (21), 385.  
428 <https://doi.org/10.1063/1.1917756>.

429 (43) Barreteau, C.; Desjonquères, M. C.; Spanjaard, D. *Theoretical Study of the Icosahedral to*  
430 *Cuboctahedral Structural Transition in Rh and Pd Clusters*; 2000; Vol. 11.  
431 <https://doi.org/10.1007/s100530070068>.

432 (44) Wei, C. M.; Cheng, C.; Chang, C. M. Transition between Icosahedral and Cuboctahedral  
433 Nanoclusters of Lead. *J. Phys. Chem. B* **2006**, *110* (48), 24642–24645.  
434 <https://doi.org/10.1021/jp063982o>.

435 (45) Aragón, J. L. Transition from Multiply Twinned Icosahedral to Cuboctahedral Symmetry  
436 in Particles of Arbitrary Size. *Chem. Phys. Lett.* **1994**, *226* (3–4), 263–267.

437 https://doi.org/10.1016/0009-2614(94)00722-5.

438 (46) Rollmann, G.; Gruner, M. E.; Hucht, A.; Meyer, R.; Entel, P.; Tiago, M. L.; Chelikowsky,  
439 J. R. Shellwise Mackay Transformation in Iron Nanoclusters. *Phys. Rev. Lett.* **2007**, *99*  
440 (8). https://doi.org/10.1103/PhysRevLett.99.083402.

441 (47) Angelié, C.; Soudan, J. M. Nanothermodynamics of Iron Clusters: Small Clusters,  
442 Icosahedral and Fcc-Cuboctahedral Structures. *J. Chem. Phys.* **2017**, *146* (17).  
443 https://doi.org/10.1063/1.4982252.

444 (48) Cheng, B.; Ngan, A. H. W. Thermally Induced Solid-Solid Structural Transition of  
445 Copper Nanoparticles through Direct Geometrical Conversion. *J. Chem. Phys.* **2013**, *138*  
446 (16), 164314. https://doi.org/10.1063/1.4802025.

447 (49) Li, G. J.; Wang, Q.; Liu, T.; Li, D. G.; Lu, X.; He, J. C. *Molecular Dynamics Simulation  
448 of Icosahedral Transformations in Solid Cu - Co Clusters*; 2009; Vol. 26.  
449 https://doi.org/10.1088/0256-307X/26/3/036104.

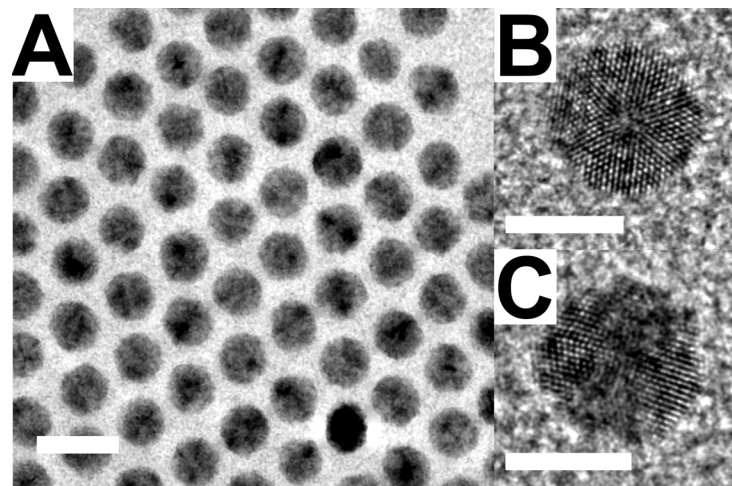
450 (50) Gao, Y.; Li, G.; Piao, Y.; Liu, S.; Liu, S.; Wang, Q. Size-Dependent Cuboctahedron-  
451 Icosahedron Transformations of Co-Based Bimetallic by Molecular Dynamics Simulation.  
452 *Mater. Lett.* **2018**, *232*, 8–10. https://doi.org/10.1016/j.matlet.2018.08.070.

453 (51) Singh, A. K. The Lattice Strains in a Specimen (Cubic System) Compressed  
454 Nonhydrostatically in an Opposed Anvil Device. *J. Appl. Phys.* **1993**, *73* (9), 4278–4286.  
455 https://doi.org/10.1063/1.352809.

456

457

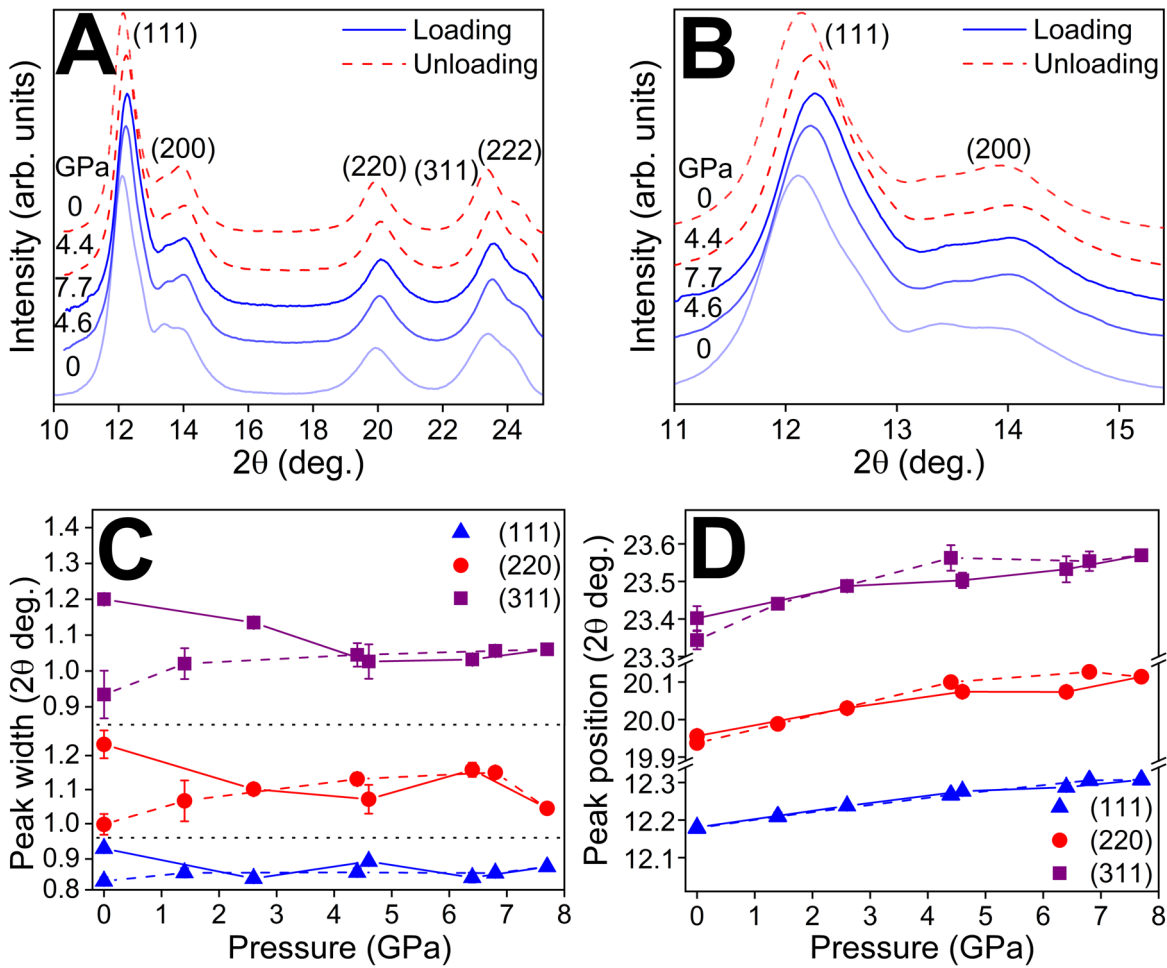
458 **Figures**



459

460 **Fig. 1. TEM images of 6 nm Au nanocrystals.** A) Bright field image of monodisperse  
461 nanocrystals. Scale bar is 10 nm. B, C) High-resolution images of icosahedral nanocrystals.  
462 Scale bar is 5 nm.

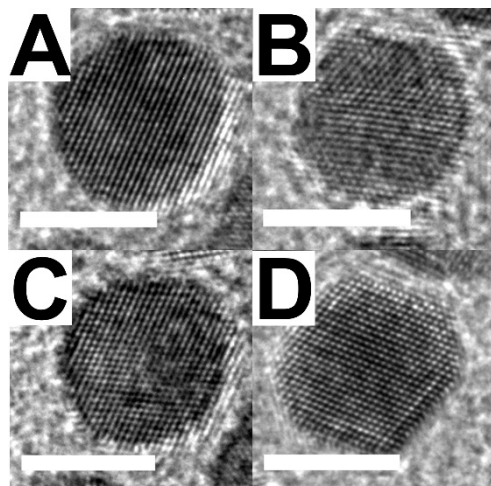
463



464

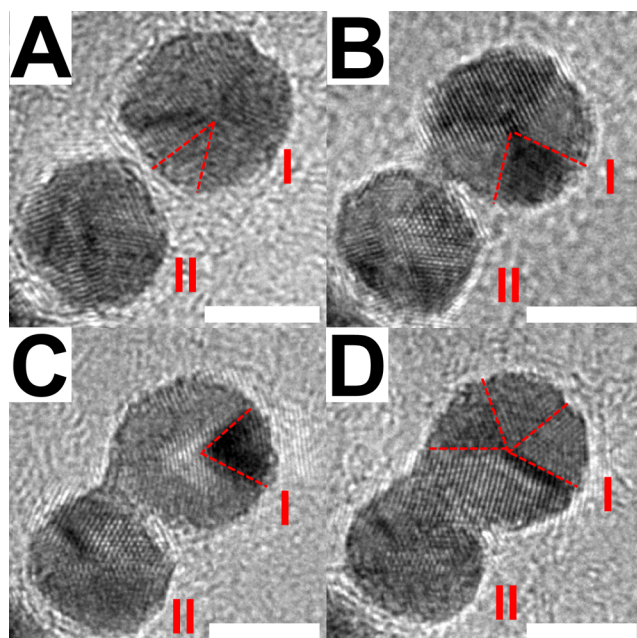
465 **Fig. 2. High-pressure XRD for 6 nm nanocrystals.** A) All diffraction peaks and B) magnified  
 466 view of (111) and (200) peaks. Change in diffraction peak C) width and D) position upon  
 467 loading (solid line) and unloading (dashed line).

468



469

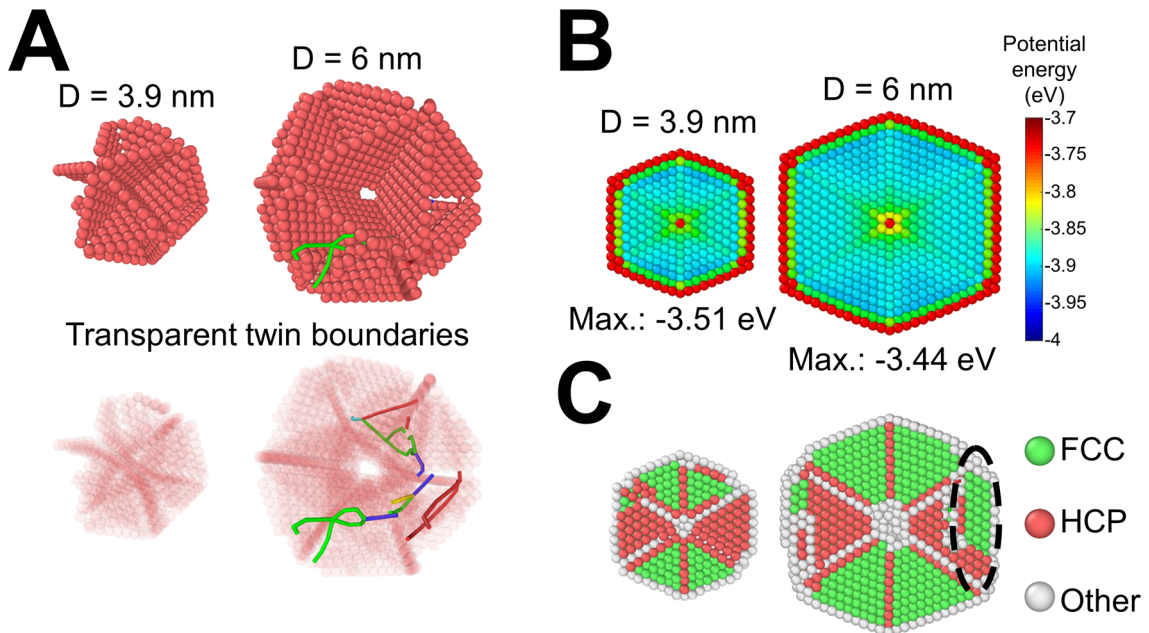
470 **Fig. 3. Post-compression TEM images of transformed single crystalline 6 nm nanocrystals.**



471

472 **Fig. 4. Snapshots from *in situ* TEM movie showing coalescence of MT nanocrystals under**  
473 **electron irradiation.** A) Nanocrystal I and II at the beginning of imaging and after B) 10 s, C)  
474 40 s and D) 70 s of electron irradiation. Red dashed line denotes the twin boundary in  
475 nanocrystal I. Scale bar is 5 nm.

476



477

478 **Fig. 5. Atomistic simulation results of 3.9 nm and 6 nm icosahedral nanocrystals.** A) Twin  
 479 boundary and dislocation structures in icosahedral nanocrystals using high temperature MD  
 480 simulations. Dislocations are formed only in the 6 nm nanocrystal due to higher pre-stress. (green  
 481 lines: Shockley partial dislocation, blue lines: full dislocation, red lines: dislocation blocked by  
 482 twin boundaries). The red atoms are at twin boundaries. Atoms in regular FCC crystal positions  
 483 are removed for visualization purposes. B) The atomic potential energy of pristine icosahedral  
 484 nanocrystals. The 6 nm nanocrystal shows higher maximum potential energy (equivalently, higher  
 485 pre-stress). C) Crystal structures of the nanocrystals after high temperature MD simulations. The  
 486 twin boundary structure in 3.9 nm is preserved without noticeable distortion, while the twin  
 487 boundary structure in 6 nm undergoes significant distortion.